Ocean Modelling 25 (2008) 120–131

Contents lists available at ScienceDirect

Ocean Modelling

journal homepage: www.elsevier.com/locate/ocemod

Modeling of mesoscale coupled ocean–atmosphere interaction and its feedback to ocean in the western Arabian Sea

Hyodae Seo [a,*], Raghu Murtugudde [b], Markus Jochum [c], Arthur J. Miller [d]

[a] Department of Atmospheric and Oceanic Sciences, University of California Los Angles, 405 Hilgard Avenue, 7127 Math Sciences Building, Los Angeles, CA 90095, USA
[b] Department of Atmospheric and Oceanic Science, University of Maryland, College Park, MD 20742, USA
[c] National Center for Atmospheric Research, 1850 Table Mesa Drive Boulder, CO 80305, USA
[d] Scripps Institution of Oceanography, University of California San Diego, La Jolla, CA 92093-0224, USA

ARTICLE INFO

Article history:
Received 28 April 2008
Received in revised form 4 July 2008
Accepted 10 July 2008
Available online 26 July 2008

Keywords:
Mesoscale air-sea interaction
Oceanography
Boundary layers
Fronts
Eddies
Regional coupled modelling

ABSTRACT

Observations of the western Arabian Sea over the last decade have revealed a rich filamentary eddy structure, with large horizontal SST gradients in the ocean, developing in response to the southwest monsoon winds. This summertime oceanic condition triggers an intense mesoscale coupled interaction, whose overall influence on the longer-term properties of this ocean remains uncertain. In this study, a high-resolution regional coupled model is employed to explore this feedback effect on the long-term dynamical and thermodynamical structure of the ocean.

The observed relationship between the near-surface winds and mesoscale SSTs generate Ekman pumping velocities at the scale of the cold filaments, whose magnitude is the order of 1 m/day in both the model and observations. This additional Ekman-driven velocity, induced by the wind-eddy interaction, accounts for approximately 10–20% of oceanic vertical velocity of the cold filaments. This implies that Ekman pumping arising from the mesoscale coupled feedback makes a non-trivial contribution to the vertical structure of the upper ocean and the evolution of mesoscale eddies, with obvious implications for marine ecosystem and biogeochemical variability.

Furthermore, SST features associated with cold filaments substantially reduce the latent heat loss. The long-term latent heat flux change due to eddies in the model is approximately 10–15 W/m^2 over the cold filaments, which is consistent with previous estimates based on short-term in situ measurements. Given the shallow mixed layer, this additional surface heat flux warms the cold filament at the rate of 0.3–0.4 °C/month over a season with strong eddy activity, and 0.1–0.2 °C/month over the 12-year mean, rendering overall low-frequency modulation of SST feasible. This long-term mixed layer heating by the surface flux is approximately ±10% of the lateral heat flux by the eddies, yet it can be comparable to the vertical heat flux. Potential dynamic and thermodynamic impacts of this observed air–sea interaction on the monsoons and regional climate are yet to be quantified given the strong correlation between the Somalia upwelling SST and the Indian summer monsoons.

1. Introduction

The variability in the western Arabian Sea is largely characterized by seasonally reversing monsoonal winds, which drive an intense oceanic response off the coast of Africa and Arabia. Southwesterly winds during the summer monsoon drive the narrow northeastward Somali Current, a northern Indian Ocean western boundary current (Schott and McCreary, 2001). Off the Horn of Africa, the Somali Current separates from the coast to form a warm, anti-cyclonic recirculation gyre, often referred to as the Great Whirl. Summer monsoon winds are upwelling favorable and induce coastal upwelling and a filamentary structure of recently upwelled waters. Flowing along the rim of the Great Whirl recirculation gyre, the upwelled water reaches 600 km offshore in the form of a cold filament (e.g., Fischer et al., 2002). The temperature difference between the warm ambient water and the cold filaments exceeds 2–3 °C along the Omani coast (Fischer et al., 2002) and more than 5 °C along the coast of Africa (Schott, 1983; Vecchi et al., 2004).

Recent satellite observations have revealed intense air–sea coupled feedbacks occurring over small-scale SST structures, which appear to be common features throughout the global ocean (Chelton et al., 2004; Xie, 2004; Small et al., 2008). The western Arabian Sea is no exception, where the aforementioned observed mesoscale SST structures perturb the stability of the atmospheric boundary

* Corresponding author. Current address: International Pacific Research Center, University of Hawaii Manoa, Honolulu HI 96822, USA. Tel.: +1 310 206 3743; fax: +1 310 206 5219.
E-mail address: hyodae@atmos.ucla.edu (H. Seo).

1463-5003/$ - see front matter © 2008 Elsevier Ltd. All rights reserved.
doi:10.1016/j.ocemod.2008.07.003

layer and the Somali Jet that directly passes over them during summer. From satellite data and in situ observations, Vecchi et al. (2004) identified a large response in the near-surface winds and turbulent heat fluxes to the mesoscale SST patterns. The most notable finding of their study is the generation of Ekman upwelling and downwelling velocities following the cold filaments. This small-scale Ekman velocity is in addition to the Ekman velocity driven by the large-scale wind field, and is induced by the SST-wind covariability at oceanic mesoscales (Chelton et al., 2001; White and Annis, 2003; Small et al., 2008). Following the timescales of oceanic eddies, these additional Ekman pumping velocities persist over a month with typical amplitude of 1 m/day, which could be large enough to explain the observed thermocline variability associated with the cold filaments (Vecchi et al., 2004). There is also a large damping effect on SSTs by the latent heat fluxes in the Arabian Sea (Weller et al., 1998), where the ship track data reveal that mesoscale eddies substantially alter latent heat flux variability (Vecchi et al., 2004).

These previous studies have suggested that summertime mesoscale air–sea interaction in the western Arabian Sea could have a large impact on the dynamics and thermodynamics of the regional ocean. However our understanding of this feedback effect on the ocean remains limited, primarily because the observations and numerical models fail to capture realistic ocean–atmosphere coupling on ocean mesoscales. In the present paper, we attempt to answer such questions by analyzing a 12-year-long high-resolution (1/4°) ocean-atmosphere coupled model simulation, focusing on the western Arabian Sea.

Using the regional coupled modeling approach, we previously studied similar processes occurring over the region of tropical instability waves (TIWs) in the tropical Pacific and Atlantic Oceans (Seo et al., 2007a; Seo et al., 2007b), where the observations have shown that large anomalies of SST generated by these waves induce substantial perturbations in the heat and momentum fluxes at the air–sea interface (Liu et al., 2000; Chelton et al., 2001; Thum et al., 2002; Hashizume et al., 2002). The SCOAR model suggested that the local coupling of wind and heat flux to the TIW-induced SSTs exerts a damping effect on the dynamics and thermodynamics of the waves. The underlying physics is identical between the western Arabian Sea mesoscale eddies and the TIWs, except that in the former case the *mean* structure is what brings about the coastal upwelling and mesoscale air–sea interaction, while TIWs are essentially a deviation from the mean circulation. Hence, following Vecchi et al. (2004), we focus on the monthly averaged fields of the model output to find the coherent mesoscale coupled variability.

The following section provides some details of the model experiment. Section 3 provides the general description of the coupled features simulated in the model. In section 4, dynamic feedback effects are discussed, and Section 5 explores the low-frequency rectification effect by the latent heat flux on the SSTs, followed by the discussion and conclusion in Section 6.

2. Model and experiment

The coupled model used for the present study is the Scripps Coupled Ocean–Atmospheric Regional (SCOAR) model, which couples two well-known, state-of-the-art regional atmospheric and ocean models through a flux-SST coupler (Seo et al., 2007a). The atmospheric component is the Experimental Climate Prediction Center (ECPC) Regional Spectral Model (RSM, Juang and Kanamitsu, 1994) and the ocean is represented by the Regional Ocean Modeling System (ROMS, Haidvogel et al. 2000; Shchepetkin and McWilliams, 2005). Details of each component of the regional model and information on the flux coupler can be found in Seo et al. (2007a).

In this study, the SCOAR model is set up for the entire Indian Ocean from 30°E–112°E and 30°S–38°N, extending from eastern Africa to the eastern Indian Ocean. The horizontal resolution is identical, namely, 0.26° for both the ocean and the atmosphere, which is sufficient to resolve important mesoscale oceanic and atmospheric processes. One of the advantages of using identically fine grids is that mesoscale coupled feedbacks can be best captured without the necessary smoothing effect on SST, such that the atmosphere actually can *see* the eddies. Moreover, one can avoid interpolation errors of fluxes and SSTs that are introduced through the inconsistent coastlines on non-contiguous grids (Seo et al., 2008).

The initialization and forcing procedures for the current simulation are as follows. The ocean model is first spun up for 8 years with a monthly climatology of atmospheric forcings (da Silva et al., 1994) and monthly climatological oceanic boundary conditions (Conkright et al., 2002). The end state from the spin-up forced ocean run is used for the initial condition for ROMS in the coupled mode. RSM in the coupled run is initialized on January 1st of 1993 using NCEP/DOE Reanalysis 2 (RA, Kanamitsu et al., 2002), which is also used to provide the low-wave number atmospheric flows over the domain. RSM employs a scale-selective spectral damping technique (Kanamaru and Kanamitsu, 2007) to ensure that the large-scale circulation (larger than 1000 km) remains close to the specified base fields. Note that the oceanic and atmospheric features of interest for this study are significantly smaller than this length scale, and hence are free to evolve without any large-scale constraint. The coupled run is performed from 1993 to 2006 with a daily exchange of fluxes (total heat flux, net freshwater flux, downward shortwave radiation, and u-, v-momentum fluxes) and SST. From the 14-year simulation, the last 12 years of the model are analyzed in this study with a focus on the western Arabian Sea during the SW monsoon.

For the analysis of the present study, the daily output fields are 3-day averaged to reduce atmospheric–oceanic noise. Then a 10° longitude zonal highpass filtering is used to highlight the covariability of the atmosphere and ocean on oceanic filamentary scales. Some uncertainty can be introduced due to the zonal spatial filtering near the coastal boundary. In some cases (e.g., Fig. 3), we applied 10° highpass filtering parallel to the coast (southwest to northeast) to minimize these errors. The quantities evaluated in this study can be somewhat dependent on the chosen filtering technique, thus the magnitudes cannot be considered absolute numbers. However, different filtering methods do not alter our basic conclusions, as long as such filtering retains the scales of oceanic eddy features and their covariability with the atmosphere.

3. Local ocean–atmosphere covariability

This section discusses the mean structure of the simulated summer monsoon. An extensive review of the observed circulation can be found in Schott and McCreary (2001), and its update, Schott et al. (2008). Fig. 1 shows the mean atmospheric and oceanic quantities for August 2002 over the western Arabian Sea from the model, along with the observed SST and surface wind fields (Fig. 1d). We show the one-month averaged fields because the typical decay time-scales of SST and wind responses are of the order of a month (Fischer et al., 2002; Vecchi et al., 2004). The month of August in 2002 is chosen because both model and satellite images of SST (Vecchi et al., 2004) exhibit the occurrence of strong coastal upwelling and cold filaments, which is the crucial precursor to the SST influences on the surface wind fields during the southwest (SW) monsoon. Note that the large-scale monsoon index generally indicates the summer of 2002 as a weak monsoon year (e.g., Murtugudde et al., 2007; Straus and Krishnamurthy, 2007). The choice of other months reveals essentially same patterns with varying amplitudes.

With the onset of the summer monsoon, the Somali Jet appears along the coast of east Africa (Fig. 1a and d), which is a sur-

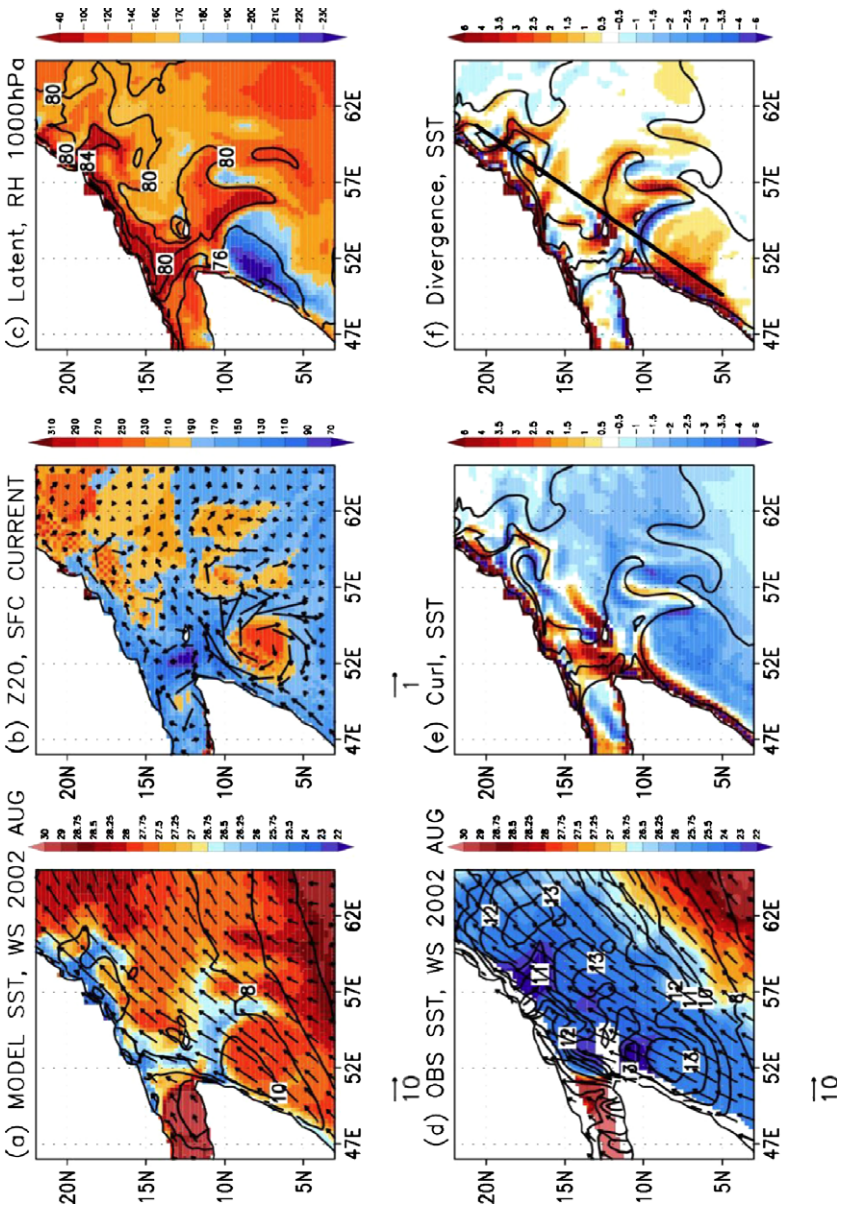

Fig. 1. Averaged quantities for August 2002 from the model simulation: (a) SST (°C, shaded), 10-m wind vectors (m/s), and wind speed (m/s, contours, CI=1 m/s), (b) depth of 20C isotherm (m, shaded), surface current vectors (m/s) (c) latent heat flux (W/m^2, positive downward, shaded), and 1000 hPa relative humidity (contours from 72 to 84 with CI = 4), (e) wind stress curl (N/m^2/10^7 m, shaded), and (f) wind stress divergence (N/m^2/10^7 m, shaded). Averaged SST from TRMM Microwave Imager (TMI) and 10-m wind from QuikSCAT scatterometer are also shown in (d). Contours in (e and f) are SST isotherms of 26, 27, 28 °C. The reference vector for (a and d) is 10 m/s and for (b) is 1 m/s. The black solid line in (f) denotes the section shown in Fig. 3.

face expression of the seasonally reversing Findlater Jet (Findlater, 1969). The SW monsoon wind and Somali Jet are upwelling favorable, inducing intense coastal upwelling along the coast of Somalia and Oman. Forced with this SW monsoon flow, a narrow, swift Somali Current develops along the coast and separates around 9°N to form the Great Whirl, an anti-cyclonic eddy off the Horn of Africa (Bruce, 1970; Schott et al., 1997). The Great Whirl persists until the late summer even after the SW monsoonal winds wither (Schott, 1983; Schott and McCreary, 2001). The secondary anti-cyclonic eddy (represented by a shoaled thermocline at 57°E, 10°N) and cold wedge between this and the Great Whirl are also seen in Fig. 1b. The Somali Current section associated with the Great Whirl exceeds 2 m/s (Swallow and Bruce, 1966; Schott, 1983; Molinari et al., 1990), forming almost a closed recirculation gyre (Schott, 1983; Schott and McCreary, 2001; Wirth et al., 2002).

The Great Whirl is quasi-stationary and transports cold, upwelled water (<20 °C from the satellite observations) from the coast offshore (as seen from the satellite imagery, e.g., Brown et al., 1980), to the east until 55°E and then to the south at 5°N. The SST difference between the warm Great Whirl and the cold wedges at its periphery in the satellite observations exceeds 2 °C zonally and as much as 5 °C meridionally over 5° longitude/latitude ranges (Vecchi et al., 2004). Note that the simulated summertime monsoon winds are much weaker than the NCEP RA2 winds (Fig. 2a and b). In combination with the weaker evaporation and cooling effect by oceanic heat advection (Fischer et al., 2002; de Boyer Montégut et al., 2007), the weaker winds in the model lead to a large warm bias in upwelled water and the cold filaments (Fig. 2c and d). The reason for weaker winds and warm bias in the model is not clear, and deserves the further investigation, which is beyond of the scope of current study. Although the SST

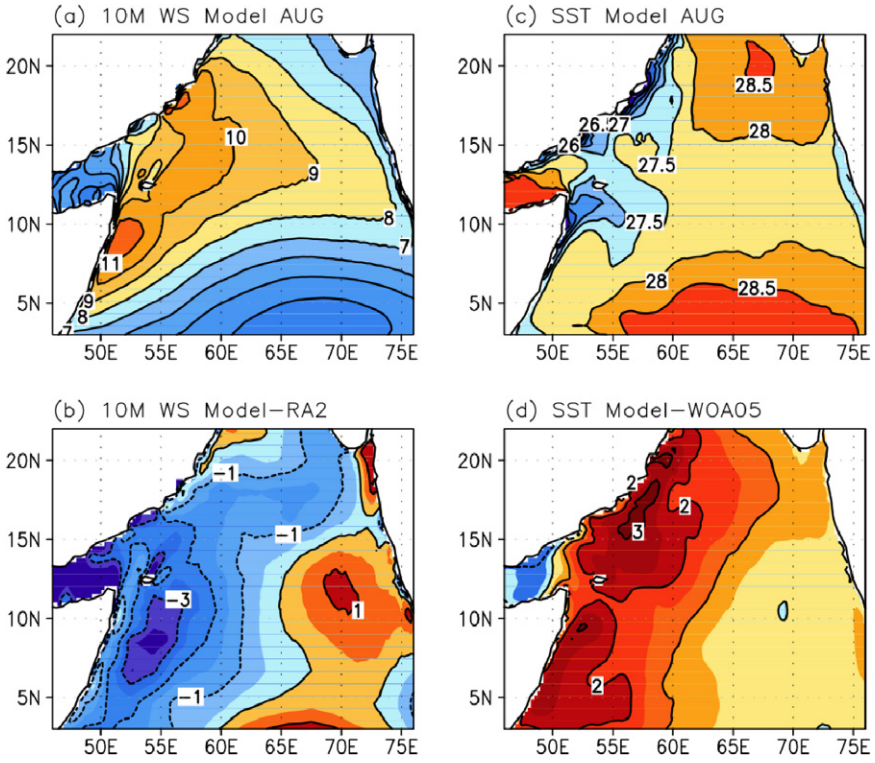

Fig. 2. Comparison of 12-year August mean (left) 10-m wind speed and (right) SSTs. (a) Model wind speed and (b) model SST, (c) wind speed difference between model and NCEP/DOE Reanalysis 2 (1995–2006), and (d) SST difference between model and World Ocean Analysis climatology.

difference between the upwelled and the ambient water in the model is smaller than in the observations roughly by half, the spatial pattern of warm Great Whirl and cold filaments remains qualitatively consistent with the observations, and as shown in the following, the coupling intensity remains realistic.

The large SST drop across the northern and eastern flank of the Great Whirl and the steady SW monsoon winds cause a distinct atmospheric response. Maximum wind speed is co-located with the Great Whirl, and the subsequent drop in wind speed of >1 m/s clearly mimics the underlying distribution of SST (Fig. 1a and d). The verisimilitude of horizontal distribution of SST and wind speed over the coastal upwelling system in the western Arabian Sea can in part be explained by the role of SST in modulating the stability of atmospheric boundary layer and the subsequent turbulent mixing of momentum and moisture. This process, originally suggested by Wallace et al. (1989) and Hayes et al. (1989), is generally accepted as the most viable hypothesis whereby ocean eddies exert an influence on the atmospheric boundary layer on many time scales (See the review paper by Small et al., 2008, and the references therein).

In addition to the direct wind-SST coupling, the narrow SST gradients produce large wind stress curls and divergences at the sea surface. As described in Chelton et al., 2001; see also Seo et al., 2007a) in the TIW region, perturbation wind stress curls are generated along the SST gradients when winds blow parallel to the isotherms. Similarly the north–south elongated cold wedges between the neighboring warm eddies (55°W 10°N in Fig. 1a for example), together with a component of monsoon flow that blows along the cold filaments, provide a favorable condition for generating an offshore wind stress curl maximum (Fig. 1d). More distinctive are the alternating bands of wind stress convergence and divergence upwind and downwind of the filament at the northern rim of the Great Whirl (Fig. 1e). This is because it is in this region that the vectors of persistent wind and SST gradients are parallel and should be associated with the generation of maximum divergence as is seen in the western part of the cusps of TIWs (Chelton et al., 2001). The observations of global SSTs and ocean winds from Tropical Rainfall Measuring Mission (TRMM) Microwave Imager (TMI) and the Quick Scatterometer (QuikSCAT) indicate that these open-ocean wind stress derivatives are a ubiquitous feature occurring throughout the global ocean (Chelton et al., 2004; Xie, 2004).

The coherent variability in SST and wind speed also explains the variability in turbulent heat fluxes (Fig. 1c). Our convention is positive heat flux downward, warming the ocean. Over the Great Whirl, where SST is warm and wind speed is at its maximum, mean latent heat loss is >220 W/m^2. On the other hand, over the cold wedges, latent heat loss is reduced to 40 W/m^2 (Fig. 1c). Likewise, sensible heat flux change, albeit much weaker in amplitude, also mimics the difference in underlying SST and air temperature changes (not shown) with an enhanced sensible heating over the cold filaments. Since the magnitudes of sensible heat flux are generally smaller compared to the latent heat flux (Weller et al., 1998), they will not be discussed in detail.

Latitude–time diagrams in Fig. 3 further illustrate the spatial and temporal covariability of the direct and indirect coupling of SST and the atmosphere. A narrow cold filament develops around 10°N in June with the onset of monsoonal winds, then quickly strengthens in the middle of July to a large negative anomaly of <−1 °C. The secondary weaker cold filament appears further north around 18°N, extending from the Omani coast. The meridional SST gradient in the boundary between the Great Whirl and cold filament exceeds 1.6 °C over a distance less than 1° in latitude. Wind anomalies demonstrably co-evolve with these SST features, with the wind speed enhanced by 0.6 m/s over the Great Whirl and markedly reduced over the cold filament by <−0.4 m/s (Fig. 3b). This is also the case for the cold filament from the coast of Oman, which reduces the positive wind anomaly close to 0. Note that the ~0.6 m/s meridional component of the anomalous wind at 9°N switches its direction to northeasterly following the underlying SST pattern at 10°N, with a large change in the zonal wind compo-

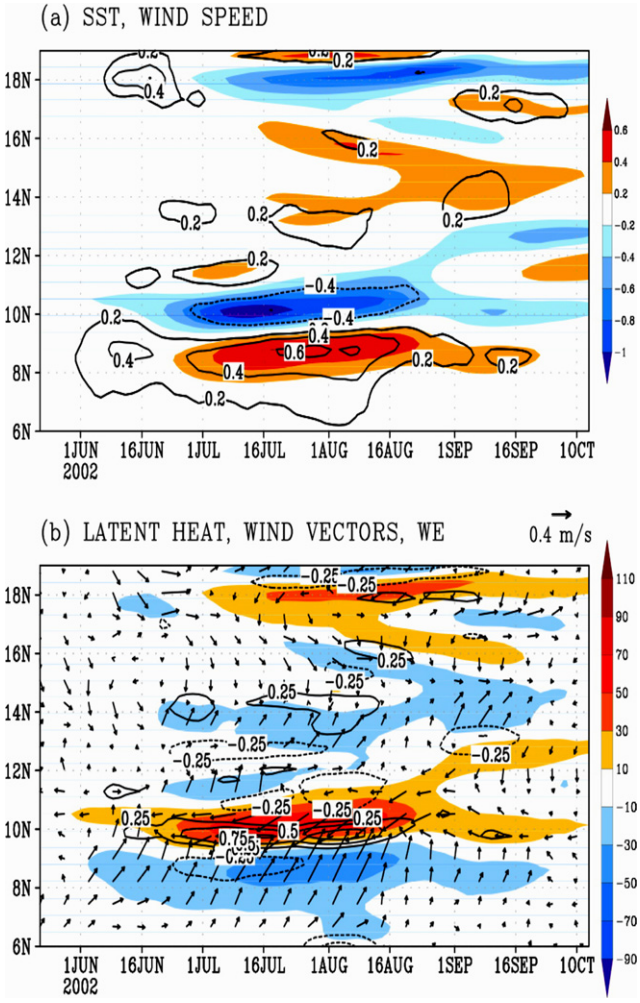

Fig. 3. Time–latitude plots of (top) SST (°C, shaded) and wind speed (m/s, contoured with CI=0.2 m/s), and (bottom) latent heat flux (shaded, W/m^2), 10-m wind vectors (m/s) and Ekman pumping velocities (m/day, contoured with CI = 0.25). The fields shown are spatially highpass filtered (10°) parallel to the coast (southwest to northeast) and then averaged within 2° longitude from the coast.

nent. Changes in SST and wind speed efficiently modify the latent heat fluxes and Ekman pumping velocities shown in Fig. 3b. Latent heat flux is out-of-phase with the SSTs, indicating local damping effects of SST (Liu et al., 2000, 2007; Thum et al., 2002; Seo et al., 2007b). Perturbation Ekman pumping velocities of up to 1 m/day are generated in the regions of maximum SST gradient (Vecchi et al., 2004).

Fig. 4 presents the binned scatterplots of these quantities (June–September, 1995–2006) to quantify the relationship between mesoscale SST variability and the near-surface fields. When zonally highpass filtered, a linear, positive relation between SST and wind speed emerges. The slope of the binned averages, s, known as the coupling coefficient (Chelton et al., 2001), is about 0.5 m/s/°C (Fig. 4a). Considering the approximately 2 °C drop of SST from the Great Whirl to the cold filament in the model, wind speed varies by 1 m/s when the SW monsoon winds pass over the Great Whirl and cold filament. Note that this relation is not clear without filtering (Fig. 4c). Latent heat flux in Fig. 4b is negatively correlated with the SST, confirming that ocean mesoscale features drive the perturbations in latent heat flux that act to damp the SST. This mesoscale damping effect is estimated at about -55 W/m^2 for a 1 °C change in SST by eddies. Comparing with the background damping effect of 25 W/m^2/°C (Fig. 4d), the eddies substantially alter the heat flux input into the ocean (Jochum and Murtugudde, 2006). The potential long-term effect on the SST is discussed in Section 5.

4. Ekman pumping velocities and thermocline variability

While the signal of wind stress divergence is much larger than wind stress curl (Fig. 1), wind stress curl is of particular importance to the ocean circulation because it is related to open ocean Ekman pumping. Previous studies have suggested the possibility of dynamic feedback from this additional wind stress curl through Ekman dynamics (Chelton et al., 2004). Seo et al. (2007b), for example, have evaluated TIW-induced atmospheric feedback on to the waves, revealing damping effects through wind speed adjustment to the SST anomalies. In their study, however, the effects of TIW-induced Ekman pumping velocity back on the instability of the waves were not clear because the maximum wind stress curls are generated close to the equator. In the western Arabian Sea, however, the perturbation wind stress curl occurs over the eddies sufficiently far from the equator, and the corresponding magnitudes of Ekman pumping exceed ±1 m/day on monthly time scale (Vecchi et al., 2004).

Ekman pumping velocity discussed throughout the study is diagnosed from the wind stress of the coupled model by $w_{ek} = \nabla \times (\tau/\rho f)$, where τ is the wind stress, ρ is the density of sea water and f is the planetary vorticity. Thus the resulting vertical velocity is linear without any non-linear contribution due to the lateral change in relative vorticity of the eddies (*cf*, Mahadevan et al., 2008). The goal of this section is to quantify the importance of wind-eddy-induced linear Ekman pumping velocity compared to the total velocity of the ocean.

Fig. 5 illustrates the link between SST, Ekman pumping velocity, thermocline depth, and the mixed layer depth (MLD) for August of 2002. We use the depth of the 20 °C isotherm (Z20) as a proxy for the thermocline depth and the MLD was calculated as the depth where the temperature drops by 0.8 °C from the sea surface. The results are not sensitive to different choices of these definitions of Z20 and MLD. The typical SST distribution during the SW monsoon season is shown in Fig. 5a, where the cold filaments extend from the coast of Somalia and Oman, and are surrounded by warm waters (Fig. 5a). Closely related with these SST patterns are the Ekman upwelling velocities (Fig. 5b). The maximum mean Ekman upwelling velocity of 1.5 m/day occurs more than 600 km offshore, a distance much smaller than the scale of atmospheric synoptic variability. Since these open oceans Ekman pumping velocities are spatially confined along the narrow SST filament, SST effects on the surface winds should be the most dominant process for this feature (Chelton et al., 2007). The amplitude of Ekman velocities is comparable to the values along the coastal ocean and also in the lee of Socotra Island, which is probably driven by the wind shadow effect of the island (Xie et al., 2001). The region of large amplitudes of Ekman pumping velocity corresponds to the region of cold filaments, where the geometry between the SST gradient vectors and wind stress vectors permits generation of wind stress curl.

Fig. 5c illustrates the mean depth of the thermocline, Z20. Deepening of Z20 in the Great Whirl and the anti-cyclone in the east is large and is in fact a climatological feature, leaving a clear imprint in a map of the 12-year summertime mean (not shown). Also obvious is the rising of the thermocline toward the cold wedges (Swallow et al., 1983; Schott, 1983): mean Z20 shoals from 250 m in the Great Whirl to 150 m in the cold filaments (Fig. 5c). The map of MLD is similar, where deep MLD of 150 m over the Great Whirl shoals to within 50 m towards the east and north over the cold wedge. The thermocline signals associated with the Great Whirl and cold filament are about 100 m and the standard deviation of

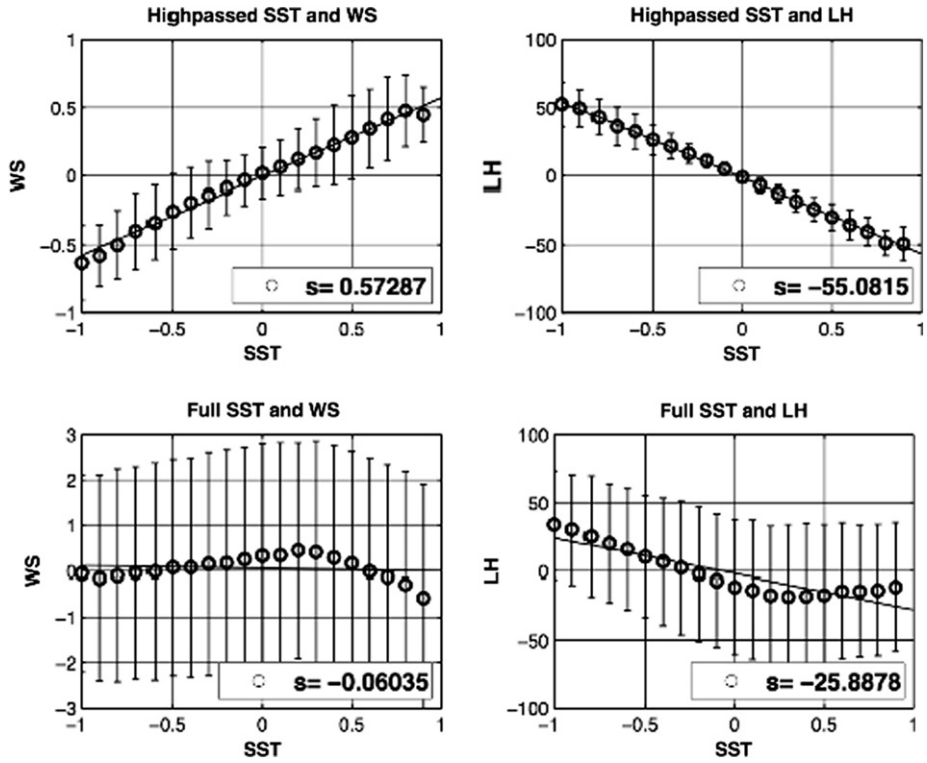

Fig. 4. Binned scatterplots of (top) highpass filtered and (bottom) full field of (left) SST and wind speed (WS) and (right) SST and latent heat flux (LH) for June-September of 1995–2006 over the region of large eddy activity (48.7°E–57.8°E and 7.4°N–13.8°N). Solid circles in the plot indicate the overall mean values within each bin for the whole period of time, and the error bars represent the ±1 standard deviations of the scatter. The solid lines through the binned means represent least squares fits of the binned means to the straight lines. The parameter, *s*, in each plot indicates the slopes of the fitted line (coupling strength).

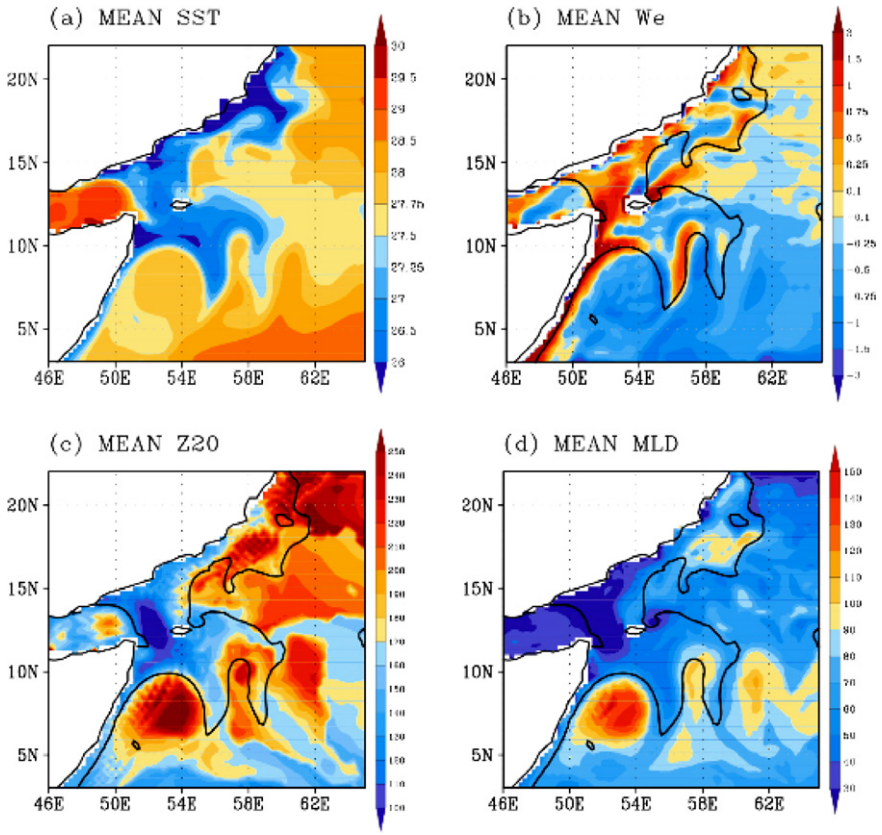

Fig. 5. Mean (a) SST (°C), (b) Ekman pumping velocities (W_e, m/day), (c) thermocline depth (Z20, m) and (d) mixed layer depth (MLD, m) for August 2002. The contour in (b–d) denotes isotherms of 27.25 °C, which represents the cold filaments.

thermocline underneath the cold filaments is about 30 m (not shown). The timescale of these Ekman pumping velocities should be similar to that of the oceanic mesoscale features, which is of the order of a month (Fischer et al., 2002). Hence the thermocline variability associated with the Ekman velocity occurring at the cold filaments is an important component for the actual thermocline depth signal (Vecchi et al., 2004). Since the evolution of the Great Whirl and cold wedges are largely dependent on the details of the mesoscale eddy field (Magnhnani et al., 1998) and oceanic intrinsic variability (Schott and McCreary, 2001; Wirth et al., 2002; Jochum and Murtugudde, 2005), this suggests that, at least in the model, mesoscale coupled processes are an important factor that affects the evolution of eddies, in support of Vecchi et al.'s view.

Fig. 6 confirms the importance of eddy-induced Ekman pumping velocities. The Fig. compares the probability density functions (PDFs) of Ekman pumping velocity computed from the mean summertime wind stresses with that due to the anomalous summertime wind stresses. O'Neill et al. (2005) and Chelton et al. (2007) used this method to demonstrate the importance of eddy-SST effects on the summertime wind stress curls in the Southern Ocean and the California Current System (CCS) region, respectively. Again, mesoscale SST has $O(1)$ impact on the anomalous Ekman pumping velocity, while the mean Ekman pumping velocity is largely governed by the broader scale structure of the SW monsoon flow. The PDFs of mean Ekman pumping velocity are shifted slightly to downwelling because SW monsoon winds induce large-scale Ekman downwelling to the south of the jet-axis (Bauer et al., 1991; Murtugudde et al., 2007). Note that the dynamic ranges of the two distributions are comparable. The RMS value of anomalous Ekman upwelling velocities of ~0.8 m/day are significant. Approximately 10% of the mean Ekman upwelling velocities exceed this RMS value, whereas greater than 18% of the anomalies (including both positive and negative) is larger than this RMS value. This result compares favorably with that of Chelton et al. (2007) in the CCS. The underlying mechanisms are identical, although the magnitudes of upwelling velocities are much larger in the western Arabian Sea.

Since a dynamic feedback effect from the SSTs is likely, it would be illuminating to conduct a similar survey of Ekman pumping velocities induced by eddies over the global ocean based on satellite measurements (*cf*, Chelton et al., 2004). It would be also worthwhile to compare this with the results from the state-of-the-art coupled climate models (Chelton and Wentz, 2005; Maloney and Chelton, 2006). Note that both fine-scale SST and mesoscale coupled feedbacks are the essential ingredients to put this process to work (Chelton and Wentz, 2005). At least in the CCS region, a high-resolution numerical weather prediction model fails to capture the essence of the observed process due to the lack of both processes in those simulations (Chelton et al., 2007).

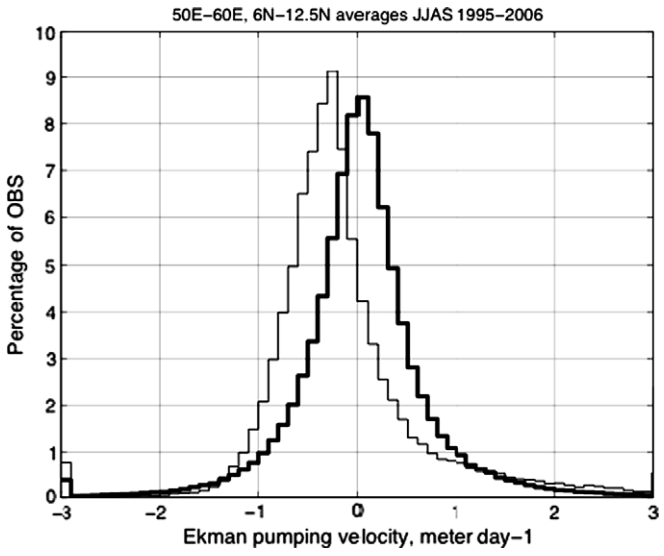

Fig. 6. Probability density functions of Ekman pumping velocities computed from (thin line) mean summertime wind stresses and (thick line) anomalous wind stresses from the monthly model climatology (1995–2006) over 50°E–60°E and 6°N–12.5°N.

5. Long-term effects of latent heat flux on the ocean

Section 3 illustrated a clear negative correlation between mesoscale SSTs and the latent heat fluxes. In this section, the low-frequency modulation of SST by latent heat is diagnosed. For Fig. 7a, we calculated latent heat flux using a conventional bulk parameterization of Fairall et al. (1996), i.e., $LH = \rho L C_H U(q_a - q_s)$, where is ρ is air density, L is the latent heat of vaporization of water, C_H, the bulk exchange coefficient, U, wind speed, and q_a, specific humidity of air and q_s, the saturation specific humidity at the temperature of the ocean surface. Note that the latent heat flux that was used in the coupled model was evaluated through the non-local planetary boundary layer physics of RSM (Hong and Pan, 1996), while the latent heat flux analyzed in this section is derived using a bulk formula based on the knowledge of SST and atmospheric variables from the coupled model. As expected, there is a slight difference, albeit not significant, in the estimates of latent heat flux shown in Fig. 1c and one that is shown in this section probably due to the non-local effects.

The 12-year June–September mean latent heat flux re-assessed from the full quantities is shown in Fig. 7a and its difference with latent heat flux computed from spatially averaged U, q_a, and q_s (5° longitude smoothing) in Fig. 7b. The negative latent heat (evaporative cooling) of 200 W/m^2 over the Great Whirl generally decreases to the north and east and the signature of cold filaments are apparent even in the long-term average field. A large difference between the full and the smoothed latent heat flux is found in the region of cold filaments along the coast, which induces on average 10–15 W/m^2 of condensational heating for the summertime, and over the Great Whirl, which experiences evaporative cooling of an even greater amount. The current model result supports the analyses of Vecchi et al. (2004) based on short-term in situ ship-track observations near the Omani coast. Using high-resolution data, they found that eddies enhance latent heat flux by 19% (10 W/m^2) when compared with the latent heat flux computed from spatially averaged data along the ship track. Their estimate relied on one realization with a strong feature near the Omani coast, yet the comparison with the current long-term analysis suggests that their estimate is robust over a long period of time and is representative throughout the whole northwestern basin over the cold filaments.

The total heat flux difference from the Great Whirl to the cold filaments is approximately 80 W/m^2 for June–September of the entire 12 years (Fig. 7c). Also note the heat gain of 80 W/m^2 in the broad region off the Omani coast (Weller et al., 1998), along with the signature of the cold filaments (greater heat flux into the ocean by 20 W/m^2). Thus a significant amount of total heat flux can be created and enter the ocean with the help of oceanic mesoscale features. Note that the difference fields of total heat flux shown in Fig. 7d closely resemble the difference map of latent heat flux (Fig. 7b), suggesting that it is the latent heat flux by eddies that is the most important source of total heat flux variability (Weller et al., 1998; de Boyer Montégut et al., 2007).

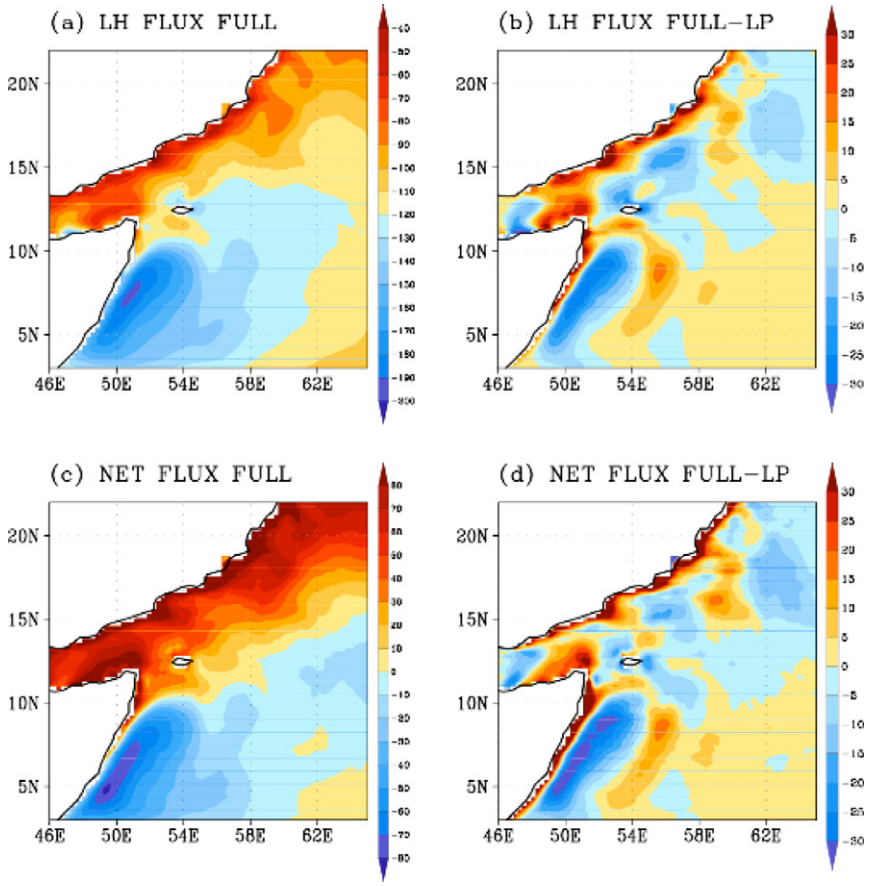

Fig. 7. (a) Latent heat (LH) flux computed from the full quantities (FULL) using the bulk parameterization, (b) difference of LH in (a) and LH computed from spatially lowpass (LP) filtered quantities (using 10° zonal moving averages) estimated for the summer months (JJAS) of 1995–2006. (Bottom) Same as top except for the total net heat flux. Positive heat flux warms the ocean.

6. Discussion and conclusions

Diagnosing the quantitative impact of mesoscale coupled ocean–atmosphere interaction on the dynamics and evolution of the oceanic circulation is not trivial, even when using a fully coupled model. One needs a suite of coupled and complementary uncoupled experiments, whereby the process of interest is tested through sensitivity experiments. All these complementary uncoupled experiments are absent here. Hence, this study remains somewhat descriptive and is guided heavily on the knowledge that was obtained from previous observations and published model simulations for the same or similar features in other regions.

In the tropical Atlantic TIW case, for example, we have shown that large amplitudes of SST anomalies induced by the waves generate substantial perturbations in the atmospheric wind fields through the same mechanisms suggested by Wallace et al. (1989) and Chelton et al. (2001). A direct response of wind speed to SST anomalies slows down the upper ocean TIW currents, thus acting as an EKE sink. However, the effects of perturbation Ekman pumping velocity remained uncertain due to the proximity of wind stress curl to the equator. Furthermore, a local negative damping effect of SST by latent heat flux was apparent over the different phases of the TIW eddies, although the oscillatory waves render the large-scale averaged effects on SST small. The current study demonstrated that the same mesoscale coupled feedback framework exists in the western Arabian Sea, with possibly larger feedback effects on the oceanic key processes.

The presence of coastal upwelling complicates assessing the feedback effects from the wind stress curl near the coast. However farther offshore, the satellite observations reveal a spatially and temporally coherent variability among the Ekman pumping, SST filament and the thermocline variability at the oceanic mesoscales during the SW monsoon (Fig. 3). Mean Ekman pumping velocity locally generated in the cold wedge is order of 1 m/day both in the observations (Vecchi et al., 2004) and the model (Fig. 5), which typically persists over a month (Fischer et al., 2002). When compared with the simulated thermocline depth of about 150 m, and the mixed layer depth of 50 m, these Ekman pumping velocities modulate the oceanic vertical structure significantly.

To illustrate this, Fig. 8b shows the ratio of mean Ekman pumping velocity shown in Fig. 5b to the mean oceanic vertical velocity at the base of the mixed layer (Fig. 8a) for August 2002. From the coast to the eastern rim of the Great Whirl, upward and downward vertical velocities of the ocean exceed ±3–4 m/day, while Ekman pumping velocities are of order of 1 m/day, which yields a ratio of the two vertical velocities of approximately 10–20%. This change of vertical velocities by mesoscale eddies makes a non-trivial contribution to the vertical structure of the upper ocean and the evolution of the ocean current. Note that in the open ocean, ocean jets and mesoscale eddies are weaker, and ocean upwelling is generally similar to the Ekman velocity (ratio exceeding 1, Fig. 8b).

A theoretical study by Lee et al. (1994) has shown that the interaction between persistent winds (like the SW monsoon wind) in the direction of an ocean jet (such as the Somali Current) and mesoscale eddies (like the cold filaments) creates deep secondary circulations and large vertical velocities through non-linear Ekman pumping, which appears to be as large as the mean Ekman pumping (Fig. 6). McGillicuddy et al. (2007) observed the large vertical

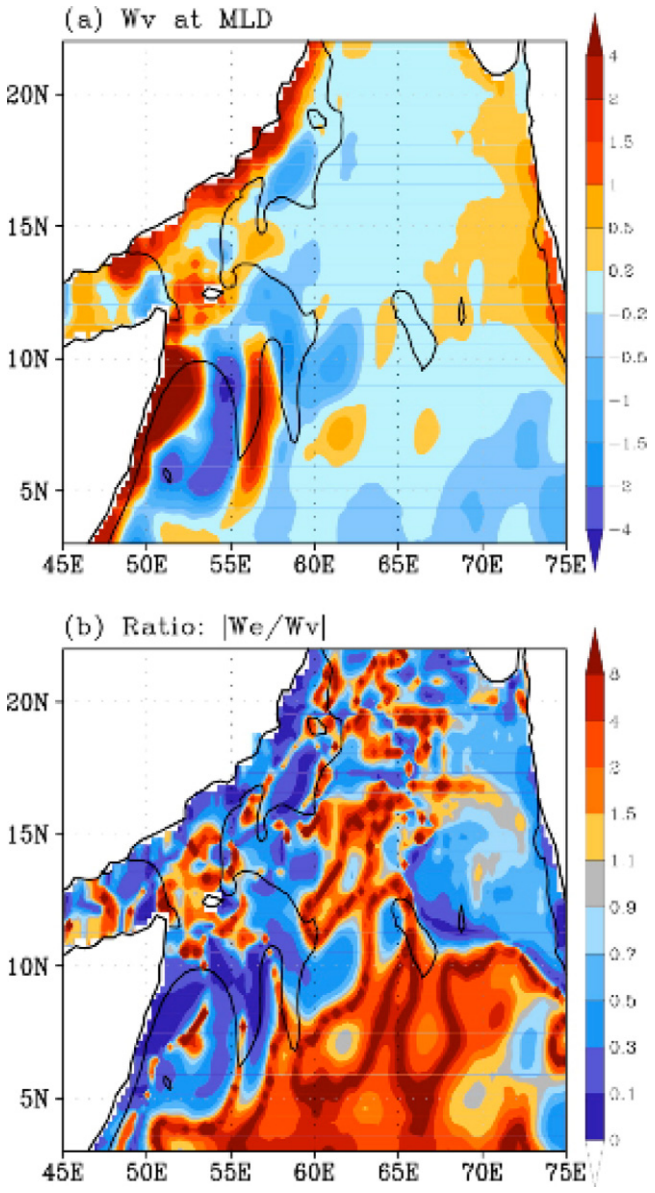

Fig. 8. (a) Mean ocean vertical velocities (W_v) at the base of the mixed layer (m/day) for August 2002. (b) The ratio of absolute values of mean Ekman pumping velocity (W_e, shown in Fig. 5b) to the absolute values of vertical velocity shown in (a). The W_e and W_v were spatially smoothed by 2° longitudes and 2° latitudes.

velocity and the associated supply of nutrient flux at the rim of anti-cyclonic mode-water eddies and proposed that eddy-wind-induced upwelling sustains the large mid-ocean plankton blooms in the subtropical ocean. Furthermore, the modeling study by Mahadevan et al. (2008) suggested that non-linear Ekman transport operating at the periphery of the eddies can be of primary importance in inducing even greater vertical velocities and nutrient fluxes along the periphery of the anti-cyclonic eddy. The SCOAR model supports the results from these previous studies and emphasizes the importance of understanding mesoscale upwelling and downwelling due to the eddy-wind interactions, which have a significant impact not only for the evolution of eddies and regional ocean dynamics, but also for the vertical nutrient flux and hence the variability of the regional ecosystem and consequent biogeochemical processes (Wiggert et al., 2005; Wiggert and Murtugudde, 2007).

Unlike the oscillating TIWs that allow the zonally/temporally averaged cancellation of latent heat fluxes over the SST anomalies, latent heat flux fields associated with the anomalies of the coastal upwelling system in the western Arabian Sea persist over monthly time scales (Fischer et al., 2002). The estimate from the model results suggests about 100 W/m^2 changes in latent heat flux occur due to typical SST variations (2 °C) from the Great Whirl to the cold filament in a 12-year mean (Fig. 4). Furthermore, latent heat flux by ocean eddies explains a large part of the total heat flux changes (Fig. 7b and d). This suggests that mesoscale SST features alter the local mean atmospheric heat flux (Jochum et al., 2007). The difference between the long-term average of latent heat flux derived from the full quantities and long-term averages of latent heat flux computed from the spatially averaged quantities resembles the underlying SST patterns, with the opposite sign (Fig. 7). The Great Whirl and the cold wedges generate an additional ±10–15 W/m^2 of latent heat flux in the 12-year mean during the SW monsoon. This long-term analysis corroborates the estimate by Vecchi et al. (2004) based on short-term in situ measurements, which indicates that cold filaments reduce latent heat loss. With the shallow mixed layer beneath the cold filaments, this will result in oceanic heat gain. How deep this heat may penetrate below the mixed layer and how that heat may further rectify the low-frequency variability in the presence of other oceanic processes in the region need further investigation.

Fig. 9 illustrates the effect of this eddy-induced latent heat flux changes on the mixed layer heat budget (i.e., $\frac{\Delta LH}{\rho c_p H}$, where ΔLH is the latent heat flux difference, ρ is density of sea water, c_p is the specific heat capacity of sea water, H is the spatially and temporally varying depth of mixed layer). Given the spatial distribution of the MLD (Fig. 5d) in the summer of 2002, the changes in latent heat flux induced by eddies result in more than 0.3–0.4 °C warming per month over the cold filament (Fig. 9a). Since the variation of SSTs in cold wedges is approximately 0.4–0.8 °C in the model for this particular season (not shown), this is an important part of the SST variability over the cold filaments. In the 12-year mean, the overall warming effect is about 0.1–0.2 °C/month (Fig. 9b), which is also a non-negligible contribution to the SST variations of the cold filaments, considering the variability of the cold filament SST for the entire 12-year summer is approximately 0.4–0.5 °C (not shown). Note that the estimates computed from the total heat flux are similar to those computed from the latent heat flux (not shown), suggesting that the latent heat flux variation is the dominant source of total heat fluxes into the ocean here (Weller et al., 1998; de Boyer Montégut et al., 2007).

Rao and Sivakumar (2000) suggested that surface heat fluxes dominate the heat balance throughout the year in the Indian Ocean. During the SW monsoon in the western Arabian Sea, however, this simple 1-dimensional heat balance breaks down (Weller et al., 2002) due to the strong cooling effect by offshore transport of temperature gradients and vertical advection, which are largely induced by the mesoscale eddies and cold filaments (Düing and Leetmaa, 1980; Lee et al., 2000; Murtugudde et al., 2000; Weller et al., 2002; Fischer et al., 2002; Shenoi et al., 2002; de Boyer Montégut et al., 2007). Fig. 10 illustrates how importantly the long-term mixed layer heating by surface flux compares with these horizontal and vertical temperature advection processes in the ocean. Fig. 10a shows the 12-year mean summertime horizontal heat flux, $-u_h \nabla T$, averaged over the mixed layer depth, where u_h is horizontal velocity and ∇ is the horizontal gradient operator. As discussed in Fischer et al. (2002), the largest cooling effect during summer is associated with the cold filaments that extend from the coast of Somalia and Oman, which in the model is estimated at roughly 2–3 K/month cooling. This is generally in agreement with the estimate from the moored array by Fischer et al. (2002), who found mixed layer horizontal heat flux of −300 W/m^2 by cold filaments in the mixed layer during July 1995. Fig. 10b shows the vertical temperature advection, $-w\frac{\partial T}{\partial z}$, averaged over the MLD. Note that

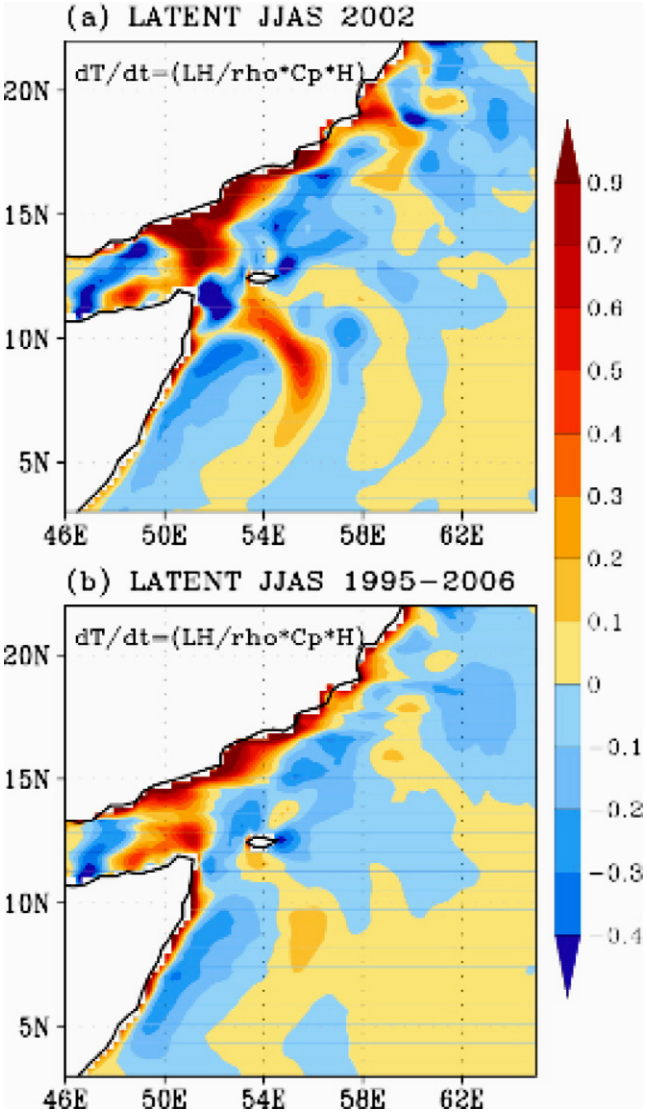

Fig. 9. Difference in temperature tendency (K/month) computed from a 1-dimensional heat balance, $\partial T/\partial t = \Delta LH/(\rho C_p H)$, where H is the space-time dependent mixed layer depth and ΔLH is the difference in latent heat flux, computed from the full quantities and low-passed quantities (see captions of Fig. 7). (a) June–September 2002 only and (b) averages of June–September, 1995–2006. The estimate based on the total heat flux difference yields similar features (not shown).

the Great Whirl is warmed by the vertical heat flux convergence at up to 1 K/month, which is roughly balanced by horizontal heat flux divergence. Note also that the vertical heat flux warms (cools) the waters upwind (downwind) region of the cold filament centered at 55°E, 7°N, which appears to correspond to the patterns of the oceanic vertical velocities (Fig. 8a) and external Ekman pumping velocities (Fig. 5b). Hence, the vertical heat flux is in part due to the Ekman pumping induced by the cold filament, and this can affect the evolution of the filaments. This generally supports the conceptual model on the evolution of fronts due to the wind-SST relation suggested by Vecchi et al. (2004, their Fig. 9), where an Ekman downwelling/upwelling-induced SST front can affect the total temperature tendency and eventually can move the SST filaments northeastward.

Fig. 10c and d show the ratio plots of mixed layer heating by surface flux to the horizontal and vertical heat flux component for 12-year summertime averages. The surface heat flux induces large mixed layer cooling over the Great Whirl (Fig. 9), which effectively reinforces the cooling effect by horizontal heat flux divergence (the ratio is toward +1 in Fig. 10c), while it largely opposes the vertical heat flux convergence (ratio toward −1 in Fig. 10d). Over the filament, the surface heat flux effect is generally ±10% compared to the horizontal heat flux, but it can be comparable to the vertical temperature flux in the cold filament (narrow high ratio centered at 55°E, 7°N). Isolating the detailed processes of the thermodynamical balance of the upper ocean is beyond the scope of this study, yet the analyses suggest the possibility of a long-term rectification effect from the eddy-induced surface heat flux on the mixed layer heat balance and hence SSTs.

The large dynamic and thermodynamic feedbacks discussed in this paper raise a potential problem in ocean modeling studies, where the observed wind and heat flux products are typically specified at the sea surface. In the observations (Vecchi et al., 2004) and the current SCOAR model, mesoscale SST features in the western Arabian sea significantly perturb surface forcing fields, which in turn can modulate the variability of the eddies and heat balance. In forced ocean models, however, the specified surface forcings derived from the observed variability are generally mismatched with the simulated SST fields, and this mismatch can be a source of error due to the mechanisms discussed throughout this paper. This problem was previously discussed in the TIWs case using the SCOAR model (Seo et al., 2007b). Hence, like many other scales of ocean circulation, the mesoscale eddies should be viewed as a fully coupled process, and given its potential for low-frequency modulation, this process needs to be properly captured or parameterized in numerical models (McC. Hogg et al. submitted to the Journal of Climate, 2008). While coupled general circulation models will eventually advance toward resolving the oceanic eddy scale, a high-resolution downscaled coupled model such as SCOAR can provide useful insight and guideline on the coupled processes and its upscaling influence on larger scales.

In addition to the feedback on the ocean, this mesoscale coupled feedback may affect the atmospheric circulation as well and consequently have a remote impact. The western Arabian Sea is a highly relevant region in this regard because of the strong statistical correlation between the SSTs, the Findlater Jet and monsoon rainfall (Shukla, 1975; Murtugudde and Busalacchi, 1999; Vecchi and Harrison, 2004; Izumo et al., in press). The observed relation between SSTs and winds on the ocean mesoscale locally enhances the wind speed over the Great Whirl while reducing it over the cold filaments. The time–latitude diagram in Fig. 3 showed a dramatic change of the anomalous meridional wind direction over the cold filament and a reduction of the zonal component of the monsoon winds. The binned scatterplots indicated the change in total wind speed of 0.5 m/s for the SST transition of 1 °C from the Great Whirl to the cold filaments in the 12-year mean. Noting that the climatological wind speed maximum of the Somali Jet is approximately 12 m/s, and is co-located with the Great Whirl, there can be a potential feedback on the structure of the low-level winds. Furthermore, the enhanced or weakened meridional winds across the front (Fig. 3b) generate large wind stress convergence and divergence (Fig. 1e). With the warm SSTs and an abundance of moisture, the near-surface convergence/divergence can alter the vertical structure of the Findlater jet (Rodwell and Hoskins, 1995), a mechanism that was recently used to describe the effect of the Agulhas Extension Meanders on the atmospheric boundary layer (Liu et al., 2007) and the Gulf Stream on the troposphere (Minobe et al., 2008). Consequently, changes in jet structure would alter basin-scale Ekman pumping velocity (Halpern et al., 1998; Halpern and Woiceshyn, 1999), thus affecting the meridional heat transport and the upper ocean heat budget (Bauer et al., 1991; McCreary et al., 1993). In combination with changes in surface evaporation over the eddies, this may in turn affect the moisture transport by the Findlater Jet and thus the seasonal precipitation in the down-

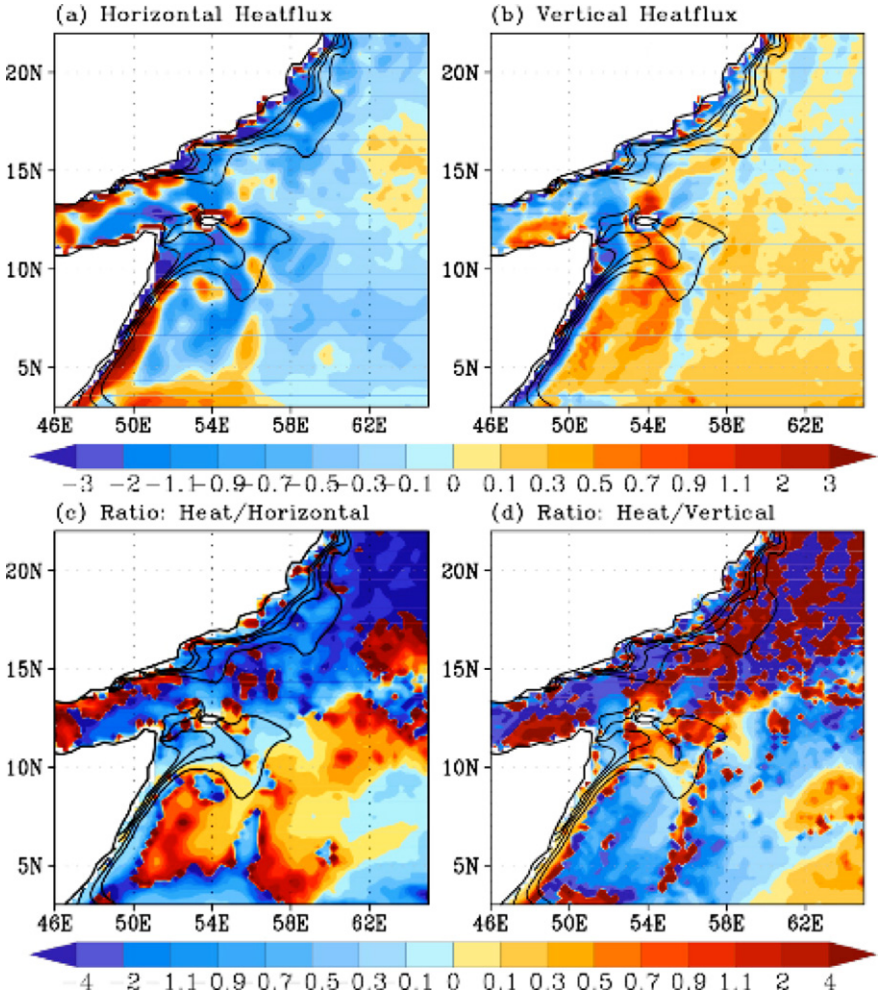

Fig. 10. (Top) (a) Horizontal heat flux (K/month), $-u_h \nabla T$ and (b) vertical heat flux (K/month), $-w\frac{\partial T}{\partial z}$, averaged from June–September, 1995–2006. (Bottom) Ratios of surface heating rate (K/month), $\frac{Q}{\rho c_p \bar{h}}$ to (c) horizontal heat flux and (d) vertical heat flux. The black contours represent isotherms from 27 to 28 °C with CI = 0.25.

stream regions in the central western Arabian Sea and the Indian subcontinent. The model setup employed here, however, with a spectral nudging technique toward NCEP RA2 (Kanamaru and Kanamitsu, 2007), does not allow us to examine the Findlater Jet structure and other large-scale implications. But our proposed hypothesis, linking mesoscale coupled feedbacks to large-scale atmospheric response, will be examined using additional regional coupled simulations and will be reported elsewhere.

Acknowledgements

This research was supported by the NOAA Climate and Global Change Postdoctoral Fellowship Program, administered by the University Corporation for Atmospheric Research. The NOAA CPO grant on Mesoscale Coupled Feedbacks is also gratefully acknowledged. Additional funding from NOAA through the Experimental Climate Prediction Center (NA17RJ1231) was also provided at Scripps. The views expressed herein are those of the authors and do not necessarily reflect the views of these agencies. We thank the anonymous reviewers for their comments and suggestions, which substantially improved the manuscript. H.S. thanks Professor Roberto C. Mechoso for mentoring and the staff in Department of Atmospheric and Oceanic Sciences at UCLA for their support. We acknowledge the Center for Observations, Modeling and Prediction at Scripps (COMPAS) for providing indispensible computer time for the coupled model simulation and H.S. is especially grateful to Caroline Papadopoulos for her excellent technical support. H.S. also thanks Shang-Ping Xie (IPRC) for his stimulating discussions and Jan Hafner (IPRC) and Steven Yeager (NCAR) for providing the QuikSCAT wind and other satellite data product. NCEP Reanalysis 2 data were provided by the NOAA/OAR/ESRL PSD, Boulder, Colorado, USA, from their Web site at http://www.cdc.noaa.gov.

References

Bauer, S., Hitchcock, G.L., Olson, D.B., 1991. Influence of monsoonally-forced Ekman dynamics upon surface layer depth and plankton biomass distribution in the Arabian Sea. Deep-Sea Res. 38, 531–553.

Brown, O.B., Bruce, J.G., Evans, R.H., 1980. Evolution of sea surface temperature in the Somali basin during the SW Monsoon of 1979. Science 209, 595–597.

Bruce, J.G., 1970. Notes on the Somali current system during the Southwest Monsoon. J. Geophys. Res. 75, 4170–4173.

Chelton, D.B., Wentz, F.J., 2005. Global microwave satellite observations of sea surface temperature for numerical weather prediction and climate research. Bull. Am. Meteor. Soc. 86, 1097–1115.

Chelton, D.B., Esbensen, S.K., Schlax, M.G., Thum, N., Freilich, M.H., Wentz, F.J., Gentemann, C.L., McPhaden, M.J., Schopf, P.S., 2001. Observations of coupling between surface wind stress and sea surface temperature in the eastern tropical Pacific. J. Climate 14, 1479–1498.

Chelton, D.B., Schlax, M., Freilich, M.H., Milliff, R.F., 2004. Satellite measurements reveal persistent small-scale features in ocean winds. Science 303, 978–983.

Chelton, D.B., Schlax, M.G., Samelson, R.M., 2007. Summertime coupling between sea surface temperature and wind stress in the California current system. J. Phys. Oceanogr. 37, 495–517.

Conkright, M.E., Locarnini, R.A., Garcia, H.E., O'Brien, T.D., Boyer, T.P., Stephens, C., Antonov, J.J., 2002. World ocean atlas 2001: Objective analysis, data statistics, and Figs: CD-ROM documentation. National Oceanographic Data Center Internal Rep. 17, 21 pp.

Da Silva, A.M., Young-Molling, C., Levitus, S., 1994. Atlas of surface marine data 1994. NOAA Atlas NESDIS 6–110, pp. 83.
De Boyer Montégut, C., Vialard, J., Shenoi, S.S.C., Shankar, D., Durand, F., Ethé, C., Madec, G., 2007. Simulated seasonal and interannual variability of mixed layer heat budget in the northern Indian Ocean. J. Climate 20, 3249–3268.
Düing, W., Leetmaa, A., 1980. Arabian Sea cooling a preliminary heat budget. J. Phys. Oceanogr. 10, 307–312.
Fairall, C.W., Bradley, E.F., Rogers, D.P., Edson, J.D., Young, G.S., 1996. Bulk parameterization of air–sea fluxes for tropical ocean–global atmosphere coupled ocean–atmosphere response experiment. J. Geophys. Res. 101, 3747–3764.
Findlater, J., 1969. A major low-level air current near the Indian Ocean during the northern summer. Q. J. R. Meteor. Soc. 95, 362–380.
Fischer, A.S., Weller, R.A., Rudnick, D.L., Eriksen, C.C., Lee, C.M., Brink, K.H., Fox, C.A., Leben, R.R., 2002. Mesoscale eddies. Coastal upwelling, and the upper-ocean heat budget in the Arabian Sea.. Deep-Sea Res. II 49, 2231–2264.
Haidvogel, D.B., Arango, H.G., Hedstrom, K., Beckmann, A., Malanotte-Rizzoli, P., Shchepetkin, A.F., 2000. Model evaluation experiments in the North Atlantic Basin: simulations in nonlinear terrain-following coordinates. Dyn. Atmos. Oceans 32, 239–281.
Halpern, D., Woiceshyn, P.M., 1999. Onset of the Somali Jet in the Arabian Sea during June 1997. J. Geophys. Res. 104, 18041–18046.
Halpern, D., Freilich, M.H., Weller, R.A., 1998. Arabian Sea surface winds and ocean transports determined from ERS-1 scatterometer. J. Geophys. Res. 103, 7799–7806.
Hashizume, H., Fujiwara, M., Shiotani, M., Watanabe, T., Tanimoto, Y., Liu, W.T., Takeuchi, K., 2002. Direct observations of atmospheric boundary layer response to SST variations associated with tropical instability waves over the eastern equatorial Pacific. J. Climate 15, 3379–3393.
Hayes, S.P., McPhaden, M.J., Wallace, J.M., 1989. The influence of sea surface temperature on surface wind in the eastern equatorial Pacific: weekly to monthly variability. J. Climate 2, 1500–1506.
Hong, S.-Y., Pan, H.-L., 1996. Nonlocal boundary layer vertical diffusion in a medium-range forecast model. Mon. Weather Rev. 124, 2322–2339.
Izumo, T., de Boyer Montegut, C., Luo, J.-J., Behera, S.K., Masson, S., Yamagata, T., in press. The role of the western Arabian Sea upwelling in Indian monsoon rainfall variability, J. Climate 45, 425.
Jochum, M., Murtugudde, R., 2005. Internal variability of Indian Ocean SST. J. Climate 18, 3726–3738.
Jochum, M., Murtugudde, R., 2006. Temperature advection by tropical instability waves. J. Phys. Oceanogr. 36, 592–605.
Jochum, M., Deser, C., Phillips, A., 2007. Tropical atmospheric variability forced by oceanic internal variability. J. Climate 20, 765–771.
Juang, H.-M.H., Kanamitsu, M., 1994. The NMC nested regional spectral model. Mon. Weather Rev. 122, 3–26.
Kanamaru, H., Kanamitsu, M., 2007. Scale-selective bias correction in a downscaling of global analysis using a regional model. Mon. Weather Rev. 135, 334–350.
Kanamitsu, M., Ebisuzaki, W., Woollen, J., Yang, S.-K., Hnilo, J.J., Fiorino, M., Potter, G.L., 2002. NCEP-DOE AMIP-II Reanalysis (R-2). Bull. Am. Meteor. Soc. 83, 1631–1643.
Lee, D.K., Niiler, P.P., Warn-Varnas, A., Piacsek, S., 1994. Wind-driven secondary circulation in ocean mesoscale. J. Mar. Res. 52, 371–396.
Lee, C.M., Jones, B.H., Brink, K.H., Fischer, A.S., 2000. The upper-ocean response to monsoonal forcing in the Arabian Sea: seasonal and spatial variability. Deep-Sea Res. II 47, 1177–1226.
Liu, W.T., Xie, X., Polito, P.S., Xie, S.-P., Hashizume, H., 2000. Atmospheric manifestation of tropical instability waves observed by QuikSCAT and tropical rain measuring mission. Geophys. Res. Lett. 27, 2545–2548.
Liu, W.T., Xie, X., Niiler, P.P., 2007. Ocean–atmosphere interaction over agulhas extension meanders. J. Climate 20, 5784–5797.
Magnhnani, V., Morrizon, J.M., Hopkins, T.S., Bohm, E., 1998. Advection of upwelled waters in the form of plumes off Oman during the Southwest Monsoon. Deep-Sea Res. II 45, 2027–2052.
Mahadevan, A., Thomas, L.N., Tandon, A., 2008. Comment on ‘‘eddy/wind interactions stimulate extraordinary mid-ocean plankton blooms”. Science 320, 448b.
Maloney, E.D., Chelton, D.B., 2006. An assessment of the sea surface temperature influence on surface wind stress in numerical weather prediction and climate models. J. Climate 19, 2743–2762.
Mc Hogg, A.C., Dewar, W.K., Berloff, P., Kravtsov, S., 2008. A mechanism of mesoscale ocean–atmosphere coupling and it's large scale effect on the ocean circulation. Submitted to. J. Climate 66, 4.
McCreary Jr., J.P., Kundu, P.K., Molinari, R.L., 1993. A numerical investigation of dynamics, thermodynamics and mixed layer processes in the Indian Ocean. Prog. Oceanogr. 31, 181–244.
McGillicuddy Jr., D.J. et al., 2007. Eddy/wind interactions stimulate extraordinary mid-ocean plankton blooms. Science 316, 1201.
Minobe, S., Kuwano-Yoshida, A., Komori, N., Xie, S.-P., Small, R.J., 2008. Influence of the gulf stream on the troposphere. Nature 452, 206–209.
Molinari, R.L., Olson, D., Reverdin, G., 1990. Surface current distributions in the tropical Indian Ocean derived from compilations of surface buoy trajectories. J. Geophys. Res. 95, 7217–7238.
Murtugudde, R., Busalacchi, A.J., 1999. Interannual variability of the dynamics and thermodynamics of the tropical Indian Ocean. J. Climate 12, 2300–2326.
Murtugudde, R., McCreary, J.P., Busalacchi, A.J., 2000. Oceanic processes associated with anomalous events in the Indian Ocean with relevance to 1997–1998. J. Geophys. Res. 105, 3295–3306.
Murtugudde, R., Seager, R., Thoppil, P., 2007. Arabian Sea response to monsoon variations. Paleoceanography 22, PA4217, doi:10.1029/2007PA001467.
O'Neill, L.W., Chelton, D.B., Esbensen, S.K., Wentz, F.J., 2005. High-resolution satellite measurements of the atmospheric boundary layer response to SST variations along the Agulhas Return Current. J. Climate 18, 2706–2723.
Rao, R.R., Sivakumar, R., 2000. Seasonal variability of near-surface thermal structure and heat budget of the mixed layer of the tropical Indian Ocean from a new global ocean temperature climatology. J. Geophys. Res. 105, 985–1015.
Rodwell, M.J., Hoskins, B.J., 1995. A model of the Asian summer monsoon. Part II: Cross-Equatorial flow and PV behavior. J. Atmos. Sci. 52, 1341–1356.
Schott, F.A., 1983. Monsoon response of the Somali Current and associated upwelling. Prog. Oceanogr. 12, 357–381.
Schott, F.A., McCreary Jr., J.P., 2001. The monsoon circulation of the Indian Ocean. Prog. Oceanogr. 51, 1–123.
Schott, F., Fischer, J., Garternicht, U., Quadfasel, D., 1997. Summer monsoon response of the Northern Somali Current 1995. Geophys. Res. Lett. 24, 2565–2568.
Schott, F.A., Xie, S.-P., McCreary, J.P., Jr., 2008. Indian Ocean circulation and climate variability. Rev. Geophys.. doi:10.1029/2007RG000245.
Seo, H., Miller, A.J., Roads, J.O., 2007a. The scripps coupled ocean–atmosphere regional (SCOAR) model. With applications in the eastern Pacific sector. J. Climate 20, 381–402.
Seo, H., Jochum, M., Murtugudde, R., Miller, A.J., Roads, J.O., 2007b. Feedback of tropical instability wave-induced atmospheric variability onto the ocean. J. Climate 20, 5842–5855.
Seo, H., Jochum, M., Murtugudde, R., Miller, A.J., Roads, J.O., 2008. Precipitation from African Easterly Waves in a coupled model of the tropical Atlantic. J. Climate 21, 1417–1431.
Shchepetkin, A.F., McWilliams, J.C., 2005. The regional oceanic modeling system (ROMS): a split–explicit. Free-surface, topography-following-coordinate ocean model. Ocean Modell. 9, 347–404.
Shenoi, S.S.C., Shankar, D., Shetye, S.R., 2002. Differences in heat budgets of the near-surface Arabian Sea and Bay of Bengal: Implications for the summer monsoon. J. Geophys. Res., 107, NO. C6, 3052, doi:10.1029/2000JC000679.
Shukla, J., 1975. Effect of Arabian Sea-surface temperature anomaly on Indian summer monsoon: a numerical experiment with the GFDL model. J. Atmos. Sci. 32, 503–511.
Small, R.J., de Szoeke, S., Xie, S.-P., O'Neill, L., Seo, H., Song, Q., Cornillon, P., Spall, M., Minobe, S., 2008. Air–sea interaction over ocean fronts and eddies. Dyn. Ocean. Atmos. 45, 274–319.
Straus, D.M., Krishnamurthy, V., 2007. The preferred structure of the interannual Indian monsoon variability. Pure Appl. Geophys. 164, 1717–1732.
Swallow, J.C., Bruce, J.G., 1966. Current measurements off the Somali coast during the southwest monsoon of 1964. Deep-Sea Res. 13, 861–888.
Swallow, J.C., Molinari, R.L., Bruce, J.G., Brown, O.B., Evans, R.H., 1983. Development of near-surface flow pattern and water mass distribution in the Somali Basin in response to the southwest monsoon of 1979. J. Phys. Oceanogr. 13, 1398–1415.
Thum, N., Esbensen, S.K., Chelton, D.B., McPhaden, M.J., 2002. Air–sea heat exchange along the northern sea surface temperature front in the eastern tropical Pacific. J. Climate 15, 3361–3378.
Vecchi, G.A., Harrison, D.E., 2004. Interannual Indian rainfall variability and Indian Ocean sea surface temperature anomalies. In: Wang, C., Xie, S.-P., Carton, J.A. (Eds.), Earth Climate: The Ocean–Atmosphere Interaction, vol. 147. American Geophysical Union, Geophysical Monograph, Washington D.C.,, pp. 247–260.
Vecchi, G.A., Xie, S.-P., Fischer, A.S., 2004. Ocean–atmosphere covariability in the western Arabian Sea. J. Climate 17, 1213–1224.
Wallace, J.M., Mitchell, T.P., Deser, C., 1989. The influence of sea surface temperature on surface wind in the eastern equatorial Pacific: seasonal and interannual variability. J. Climate 2, 1492–1499.
Weller, R.A., Baumgartner, M.F., Josey, S.A., Fischer, A.S., Kindle, J.C., 1998. Atmospheric forcing in the Arabian Sea during 1994–1995: observations and comparisons with climatology and models. Deep-Sea Res. II 45, 1961–1999.
Weller, R.A., Fischer, A.S., Rudnick, D.L., Eriksen, C.C., Dickey, T.D., Marra, J., Fox, C.A., Leben, R.R., 2002. Moored observations of upper ocean response to the monsoon in the Arabian Sea during 1994–1995. Deep-Sea Res. 49B, 2195–2230.
White, W.B., Annis, J.L., 2003. Coupling of extratropical mesoscale eddies in the ocean to westerly winds in the atmospheric boundary layer. J. Phys. Oceanogr. 33, 1095–1107.
Wiggert, J.D., Murtugudde, R.G., 2007, The sensitivity of the southwest monsoon phytoplankton bloom to variations in aeolian iron deposition over the Arabian Sea, J. Geophys. Res., 112, C05005, doi:10.1029/2006JC003514.
Wiggert, J.D., Hood, R.R., Banse, K., Kindle, J.C., 2005. Monsoon-driven biogeochemical processes in the Arabian Sea. Prog. Oceanogr. 65, 176–213.
Wirth, A., Willebrand, J., Schott, F., 2002. Variability of the Great Whirl from observations and models. Deep-Sea Res. 49B, 1279–1295.
Xie, S.-P., 2004. Satellite observations of cool ocean–atmosphere interaction. Bull. Am. Meteor. Soc. 85, 195–209.
Xie, S.-P., Liu, W.T., Liu, Q., Nonaka, M., 2001. Far-reaching effects of the Hawaiian Islands on the Pacific ocean–atmosphere system. Science 292, 2057–2060.